nature energy

ARTICLES

PUBLISHED: 31 JULY 2017 | VOLUME: 2 | ARTICLE NUMBER: 17127

Self-optimizing, highly surface-active layered metal dichalcogenide catalysts for hydrogen evolution

Yuanyue Liu[1†‡], Jingjie Wu[1‡], Ken P. Hackenberg[1‡], Jing Zhang[1], Y. Morris Wang[2], Yingchao Yang[1], Kunttal Keyshar[1], Jing Gu[3], Tadashi Ogitsu[2], Robert Vajtai[1], Jun Lou[1], Pulickel M. Ajayan[1], Brandon C. Wood[2*] and Boris I. Yakobson[1*]

Low-cost, layered transition-metal dichalcogenides (MX_2) based on molybdenum and tungsten have attracted substantial interest as alternative catalysts for the hydrogen evolution reaction (HER). These materials have high intrinsic per-site HER activity; however, a significant challenge is the limited density of active sites, which are concentrated at the layer edges. Here we unravel electronic factors underlying catalytic activity on MX_2 surfaces, and leverage the understanding to report group-5 MX_2 (*H*-TaS_2 and *H*-NbS_2) electrocatalysts whose performance instead mainly derives from highly active basal-plane sites, as suggested by our first-principles calculations and performance comparisons with edge-active counterparts. Beyond high catalytic activity, they are found to exhibit an unusual ability to optimize their morphology for enhanced charge transfer and accessibility of active sites as the HER proceeds, offering a practical advantage for scalable processing. The catalysts reach 10 mA cm^{-2} current density at an overpotential of ~50–60 mV with a loading of 10–55 μg cm^{-2}, surpassing other reported MX_2 candidates without any performance-enhancing additives.

Hydrogen is a promising energy carrier and key agent for many industrial chemical processes[1]. One method for generating hydrogen sustainably is via the hydrogen evolution reaction (HER), in which electrochemical reduction of protons is mediated by an appropriate catalyst—traditionally, an expensive platinum-group metal. Scalable production requires catalyst alternatives that can lower materials or processing costs while retaining the highest possible activity. Strategies have included dilute alloying of Pt[2] or employing less expensive transition-metal alloys, compounds or heterostructures (for example, NiMo, metal phosphides, pyrite sulfides, encapsulated metal nanoparticles)[3–5]. Among available HER electrocatalyst candidates, layered transition-metal dichalcogenide (MX_2; ref. 6) catalysts based on molybdenum and tungsten have attracted substantial interest due to their low cost and high intrinsic per-site HER activity[7–15]. However, these materials are significantly limited by the density of active sites, which are concentrated at the layer edges[8,10,11]. Accordingly, significant research investment has been directed towards synthesis strategies that can expose additional active edge sites to enhance overall performance[9,11]. An alternative strategy that obviates the need for complex nanostructuring involves the development of MX_2 catalysts that are not limited to edge activity but rather exhibit intrinsic basal-plane activity. In principle, such materials could enable far greater flexibility, materials compatibility and overall performance within existing electrode designs.

Here we address this critical need by employing first-principles calculations to reveal underlying electronic factors that control the surface activity of MX_2. A simple descriptor derived from this understanding leads to the discovery of group-5 MX_2 (*H*-TaS_2 and *H*-NbS_2) electrocatalysts whose performance derives from highly active basal-plane sites. The activity exceeds all reported MX_2 candidates, reaching an HER current density of -10 mA cm^{-2} at an overpotential of ~50–60 mV with a catalyst loading of only 10–55 μg cm^{-2}. They also exhibit an unusual ability to optimize their morphology for enhanced charge transfer and accessibility of active sites as the HER proceeds, resulting in long cycle life and practical advantages for scalable processing.

Understanding the surface activity of MX_2

The HER proceeds via two steps: H adsorbs on the catalyst by $H^+ + e^- + * \rightarrow H^*$ (Volmer reaction), where $*$ denotes a catalytic site; H_2 is formed and desorbed by either $2H^* \rightarrow H_2 + 2^*$ (Tafel reaction) or $H^+ + e^- + H^* \rightarrow H_2 + *$ (Heyrovsky reaction)[16]. Among the major factors[17] that determine the HER rate is the balance between adsorption and desorption—an empirical rule known as the Sabatier principle, typified by the 'volcano plot'[2,10,16–20]. If the substrate interaction is too weak, then the Volmer reaction is inhibited; if it is too strong, then the Tafel/Heyrovsky reaction cannot proceed. The relative adsorption free energy of the H* intermediate therefore acts as an indicator of the catalytic activity, and has been widely used to evaluate HER catalyst candidates[2,10,20].

For a deeper understanding of adsorption behaviour on MX_2 (M = transition metal; X = S, Se, Te), we examine how the underlying electronic structure is modified by the presence of the H* intermediate. We find that dilute H adsorption (on the outermost X layer) leaves the profile of the electronic density of states (DOS)

[1]Department of Materials Science and Nano-Engineering, Rice University, Houston, Texas 77005, USA. [2]Materials Science Division, Lawrence Livermore National Laboratory, Livermore, California 94550, USA. [3]Department of Chemistry and Biochemistry, San Diego State University, San Diego, California 92182, USA. [†]Present address: California Institute of Technology, Pasadena, California 91125, USA. [‡]These authors contributed equally to this work. *e-mail: brandonwood@llnl.gov; biy@rice.edu

largely intact, with complete charge transfer from the adsorbate to the substrate. Consequently, its dominant effect in both metallic and semiconducting MX_2 is to populate states at or near the lowest unoccupied state (ε_{LUS})—the conduction band minimum for semiconductors or the Fermi level for metals. The general behaviour is illustrated schematically in Fig. 1a, and implies that ε_{LUS} is the key determinant of adsorption strength on MX_2 surfaces (full DOS calculations and charge densities for specific MX_2 candidates, along with descriptions of underlying physical mechanisms, can be found in Supplementary Fig. 1). We point out that this same ε_{LUS} descriptor has been recently shown to predict lithium adsorption on carbon[21], and parallels relationships observed for chlorine evolution[22,23] and oxygen reduction[24] on certain oxides. Moreover, for metallic systems, ε_{LUS} is closely connected to the workfunction, which has long been shown to correlate with HER activity on elemental metals[18]. We verified the direct correlation between ε_{LUS} and H* adsorption energy (E_a) on the basal plane for a training set of known MX_2 at a dilute concentration (see Computational details in the Methods and Supplementary Fig. 1). As shown in Supplementary Fig. 2, other probable descriptors do not exhibit the same level of correlation; in particular, the breakdown of the '*d*-band centre' rule commonly used for transition-metal catalysts probably owes to the additional contributions from *p* states of X near the Fermi level. We therefore adopt ε_{LUS} as a descriptor for selecting basal-plane-active MX_2 catalysts based on intrinsic properties. This also renders explicit evaluation of H* adsorption unnecessary, offering a computational advantage for more efficient screening.

In Fig. 1b, we apply our ε_{LUS} descriptor to all MX_2 substrates. We consider the most stable phases (*H* for group 5 and 6, *T* for group 4 and 10, *T*′ for group 7; structures are shown in Supplementary Fig. 2). We select as a target criterion for viable candidates $-6.4\,eV < \varepsilon_{LUS} < -5.5\,eV$, which corresponds to $-0.5\,eV\ H^{-1} < E_a < +0.5\,eV\ H^{-1}$ based on Supplementary Fig. 1 (this window accounts for additional contributions to the free energy of adsorption). Note that *H*-MoX_2 and *H*-WX_2 monolayers exhibit comparatively high ε_{LUS} ($>-4.5\,eV$), which leads to weak adsorption that inhibits the Volmer reaction and prevents basal-plane activity in these materials. Two general features are observed: for a given M, ε_{LUS} (and hence E_a) increases in the order S < Se < Te; and metallic MX_2 candidates (from groups 4 and 5) have lower ε_{LUS} and hence stronger E_a than semiconducting MX_2 candidates (from groups 6, 7 and 10). Among the viable candidates, the group-5 metal disulfides (*H*-VS_2, *H*-NbS_2, and *H*-TaS_2) are clearly the most promising, having a low ε_{LUS} ($<-5.8\,eV$) near the centre of our window of interest. Calculations that explicitly account for additional contributions to the free energy of H* adsorption provide further confirmation that these three materials should have high activity per basal surface site (see Computational details in Methods and Supplementary Fig. 3). We point out that these calculations demonstrate a thermodynamic preference for more dilute H adsorption at zero overpotential (Supplementary Fig. 3); this behaviour is different from Pt, which favours a higher coverage at zero overpotential. Nevertheless, we predict that high per-site activity will be retained as the overpotential is increased to access higher coverages. The potential of the group-5 metal disulfides for HER catalysis has similarly been noted in other recent theoretical analyses by explicit evaluation of H* adsorption[25,26].

Experimental verification

We successfully synthesized and tested *H*-TaS_2 and *H*-NbS_2 (see Synthesis, Material characterization, Electrode preparation, Electrochemical performance in the Methods and Supplementary Figs 4 and 5). As shown in Fig. 2, indeed both *H*-TaS_2 and *H*-NbS_2 demonstrate high HER catalytic performance as predicted. In particular, with small loading (10–55 μg cm^{-2}), they reach a current density of 10 mA cm^{-2} (a standard for comparison[3]) at

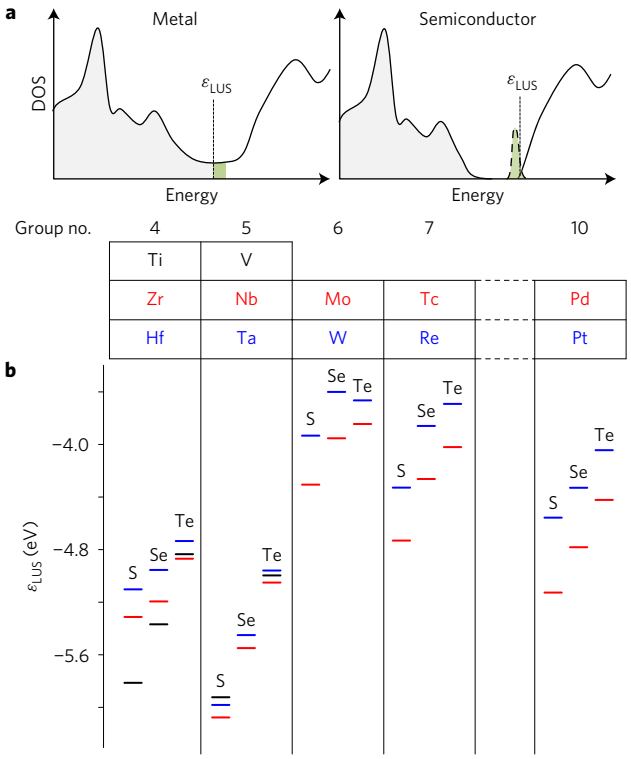

Figure 1 | Electronic origin of MX_2 surface activity and the derived descriptor (ε_{LUS}) for catalysts screening. a, Schematic of the MX_2 DOS, showing initial filled (grey) and empty states, as well as newly filled (green) states following dilute H adsorption. In metals, the Fermi level is slightly elevated, whereas in semiconductors, a shallow state appears near the conduction band edge; in each case, the newly occupied states closely follow the energy of lowest unoccupied state, designated as ε_{LUS}. **b**, Computed values of the ε_{LUS} descriptor for all MX_2 candidates. Row 4/5/6 elements are shown in black/red/blue, with the different chalcogens separated into columns within each group.

low potentials (−60 mV for *H*-TaS_2; −50 mV for *H*-NbS_2; versus the reversible hydrogen electrode (RHE)), and exhibit low Tafel slopes (37 mV dec^{-1} for *H*-TaS_2; 30 mV dec^{-1} for *H*-NbS_2) and high exchange current densities (7.8×10^{-2} mA cm^{-2} for *H*-TaS_2; 1.2×10^{-2} mA cm^{-2} for *H*-NbS_2), after thousands of cycles (5,000 for *H*-TaS_2; 12,000 for *H*-NbS_2). These performance characteristics exceed other MX_2 materials tested in this work (Fig. 2; see the Methods for synthesis and characterization details) or reported elsewhere (see Supplementary Table 1).

Although we were not able to synthesize *H*-VS_2 at this stage, *T*-VS_2 has also been found to have intrinsic activity[27], in agreement with its relatively low ε_{LUS} (∼−5.7 eV). The relevance of MX_2 crystal structure in determining catalytic activity[28–30] was also demonstrated, as Fig. 2a shows that the performance of a synthesized sample of the also-metallic *T*-TaS_2 is far inferior to the ground-state *H* phase[31,32] (this is consistent with calculations in Supplementary Fig. 1 showing that *T*-TaS_2 has a much higher ε_{LUS}). This contrasts with *T*-MoS_2, which exhibits higher overall activity than edge-active *H*-MoS_2 (refs 29,30).

The *H*-TaS_2 and *H*-NbS_2 multilayer platelets exhibit an additional unusual benefit, in that repeated catalysis of hydrogen evolution results in continual and dramatic improvement in catalytic performance before reaching steady state (for *H*-TaS_2, see Fig. 2c and Supplementary Fig. 8, as well as the potentiostatic measurements in Supplementary Fig. 11; for *H*-NbS_2, see Supplementary Fig. 9). This self-optimizing behaviour has practical advantages compared with more complex approaches

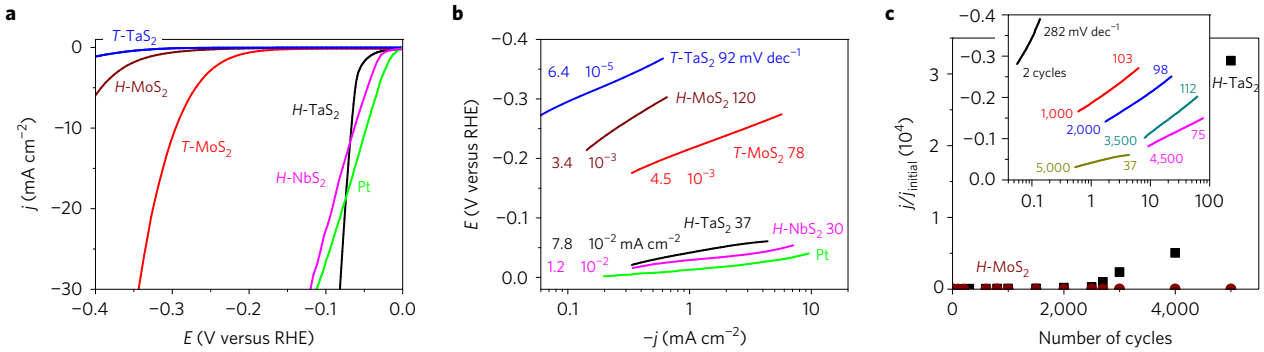

Figure 2 | HER electrocatalysis on *H*-TaS_2 and *H*-NbS_2. a, Polarization curves (iR-corrected) for *H*-TaS_2, *H*-NbS_2, *H*-MoS_2, *T*-MoS_2 and *T*-TaS_2 measured in Ar-bubbled 0.5 M H_2SO_4 with a scan rate of 5 mV s^{-1}. *H*-TaS_2 and *H*-MoS_2 were cycled for 5,000 cycles while *H*-NbS_2 was cycled for 12,000 cycles between 0.2 and −0.6 V versus RHE at 100 mV s^{-1}. Pt is included for reference. **b**, Corresponding Tafel plots for the catalysts in **a**; Tafel slopes (mV dec^{-1}) and exchange current densities (mA cm^{-2}) are shown. **c**, Comparison of current density increase during potential cycling of *H*-TaS_2 and *H*-MoS_2 between 0.2 and −0.6 V versus RHE at 100 mV s^{-1}. Data are recorded at −0.1 V for *H*-TaS_2, and −0.3 V for *H*-MoS_2 (to surmount low activity at −0.1 V). Inset shows Tafel plots (potential versus RHE (V) as a function of current density (mA cm^{-2})) of *H*-TaS_2 measured at different cycles. The Tafel slopes (mV dec^{-1}) and corresponding cycle numbers are also shown in the inset.

for optimizing MX_2 catalysts, in that it enables highly scalable processing with minimal additional treatment. Microscopy analysis indicates that the performance enhancements are associated with a morphological evolution of the catalyst. In particular, comparing atomic force microscopy (AFM), transmission electron microscopy (TEM) and scanning electron microscopy (SEM) results before and after cycling (Fig. 3 and Supplementary Fig. 12) for *H*-TaS_2 illustrates that the platelets become thinner, smaller and more dispersed. By contrast, there are no discernible changes in the local crystal structure or chemical composition of *H*-TaS_2, as confirmed by Raman spectroscopy (Fig. 4a,b), X-ray photoelectron spectroscopy (XPS) (Fig. 4c), energy-dispersive spectroscopy (EDS) and high-resolution TEM (Supplementary Fig. 12). Analogous self-optimizing morphology changes and chemical intactness are also observed for *H*-NbS_2 (see Supplementary Fig. 13).

The changes in the catalyst morphology following cycling have two key beneficial consequences for catalytic activity, which are illustrated in Fig. 4d,e. The first consequence is to shorten the interlayer electron-transfer pathways due to sample thinning. This is particularly beneficial for weakly bound layered materials, which tend to have poor electron transport along the stacking direction (see Additional characterization in the Methods and Supplementary Fig. 6). Indeed, the electrochemical impedance spectra (EIS; see Supplementary Figs 8 and 9) show that a key change following cycling is connected to decreased charge-transfer resistance (Fig. 4d for *H*-TaS_2 and Supplementary Fig. 9 for *H*-NbS_2; also see Additional characterization in the Methods for details of the equivalent circuit modelling). This translates to improved electrical conductivity in the absence of additional changes to the local chemistry. Similar conclusions can be drawn by analysing the decrease in the Tafel slope following cycling (Fig. 2c inset for *H*-TaS_2; Supplementary Fig. 9 for *H*-NbS_2), which signals a change in the rate-determining step away from the initial electron-transfer (Volmer) process as electrical conductivity improves and charge transfer becomes more facile[33].

The second consequence is to increase the effective active surface area by improving accessibility of aqueous protons to basal-plane sites. This is evidenced in the increase of the effective double-layer capacitance (Fig. 4d for *H*-TaS_2; Supplementary Fig. 9 for *H*-NbS_2), which is expected to scale roughly with the electrolyte-accessible surface area as the material is cycled (see Additional characterization in the Methods for calculation details and assumptions). Note that the very large magnitude of the capacitance increase indicates that a significant fraction of the newly accessible surface area arises from additional interior sites connected to higher porosity; these interior

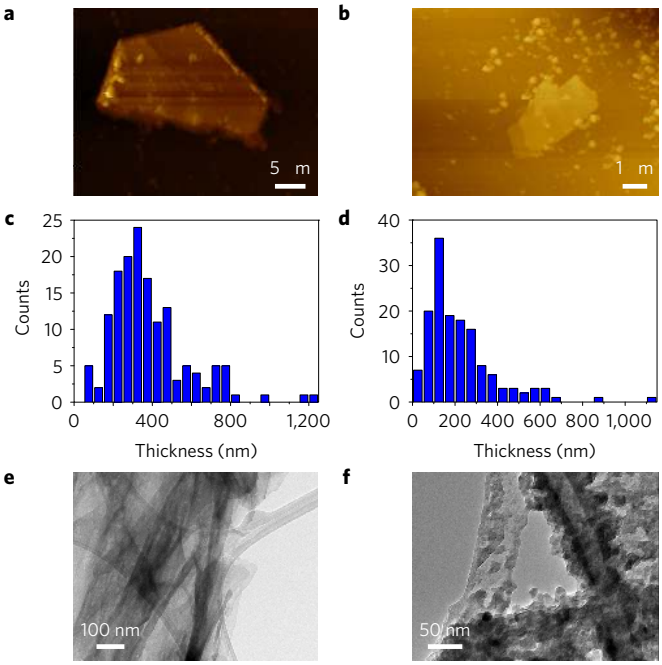

Figure 3 | Morphological evolution of *H*-TaS_2 following cycling. a,**b**, AFM images of *H*-TaS_2 before cycling (**a**) and after cycling (**b**). **c**,**d**, The corresponding statistical distributions of the thicknesses before cycling (**c**) and after cycling (**d**). **e**,**f**, TEM images of *H*-TaS_2 before cycling (**e**) and after cycling (**f**).

sites are also likely to have shorter electron-transfer pathways, offering a secondary benefit.

Consequently, both electron transport and accessible surface area are enhanced by the morphology changes, acting in concert to boost overall catalytic performance. Moreover, the current scales strongly with the solvent-accessible surface area following cycling (Supplementary Figs 8 and 9), further supporting our conclusion that active basal-plane sites are key to the observed performance (although the effective surface area is difficult to assess quantitatively[34], a qualitative increase of the surface area with cycling is nonetheless evident). Indeed, the high performance is best explained by considering both high per-site activity and a large number of active sites derived from basal-plane activity. It is worth noting that the edges of *H*-NbS_2 and *H*-TaS_2 might also have some

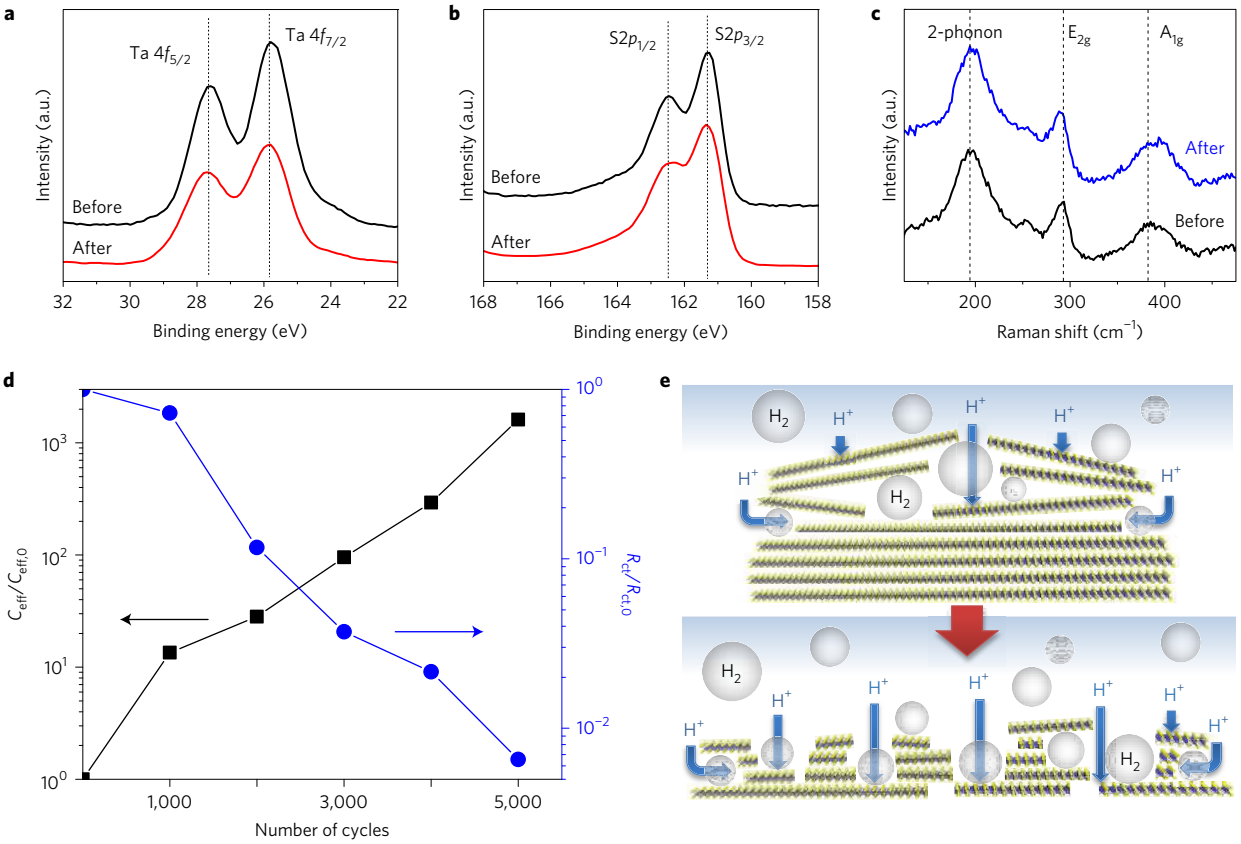

Figure 4 | Chemical intactness and origin of self-optimizing behaviour. a–c, Raman (**a**,**b**) and XPS (**c**) spectra of *H*-TaS_2 before and after cycling. **d**, Change of effective capacitance ($C_{eff}/C_{eff,0}$, where 0 denotes the initial value) and charge-transfer resistance ($R_{ct}/R_{ct,0}$) as a function of cycles. Both quantities are extracted from the EIS (see Additional Characterizations in the Methods and Supplementary Fig. 8). **e**, Schematic of the proposed mechanism for the morphology change, in which hydrogen evolution at basal-plane sites of stacked layers causes perforation and exfoliation. Plates represent MX_2 layers; spheres represent H_2 bubbles formed following HER. The top panel represents the state at an early stage of cycling, whereas the bottom panel corresponds to a late stage.

level of activity. Accordingly, we performed additional calculations, which predict a lower activity than the edges of *H*-MoS_2 (see Supplementary Discussion and Supplementary Fig. 18). Therefore, the better overall performance of *H*-NbS_2 and *H*-TaS_2 compared with *H*-MoS_2 must have leading contributions from other factors, which also suggests the presence of basal-plane activity.

Moreover, inductively coupled plasma mass spectrometry, CO stripping voltammetry (see Tests for Pt contamination in the Methods and Supplementary Fig. 14) and XPS survey scan (Supplementary Fig. 15) rule out the possibility that the high catalytic activity might instead arise from extrinsic contamination (for example, by Pt), confirming that the basal-plane activity is indeed intrinsic.

We propose that the high basal-plane activity is directly responsible for the self-optimizing morphological changes. Because *H*-TaS_2 and *H*-NbS_2 are weakly bound layered materials, H_2 produced at basal-plane sites between layers becomes trapped and perforates or peels away layers to escape, resulting in a thinner and more porous catalyst (Fig. 4e). This mechanism is analogous to reports of lithium intercalation and reaction with water in MX_2, where hydrogen gas produced between layers can cause exfoliation and fracturing[29]. It is also consistent with the observation that graphene can be delaminated from metal substrate by electrochemical H_2 bubbling[35,36]. In fact, electrochemical H intercalation and exfoliation of *H*-TaS_2 have been reported in early literature (although a different exfoliation mechanism is suggested)[37,38]. Reliance on basal-plane activity would also explain why the same improvements are not seen in edge-active *H*-MoS_2 (Fig. 2c).

Conclusion

In summary, we present highly basal-plane-active MX_2 electrocatalysts for HER, based on theoretical prediction and experimental validation. The success was facilitated by a fundamental understanding of underlying electronic motivations, from which an appropriate descriptor was devised. This descriptor helped us to computationally identify MX_2 materials with intrinsic basal-plane activity and hence a higher theoretical density of active sites compared with edge-site-limited counterparts. This leads to improved catalyst performance, as verified by direct measurements on synthesized samples of *H*-TaS_2 and *H*-NbS_2. We also find that these materials exhibit unusual self-optimizing performance as they catalyse hydrogen evolution, which derives from beneficial morphological changes that enhance charge transfer and accessibility of active sites. As a result, high performance can be achieved with minimal catalyst loading and processing, offering significant practical advantages for scalability and cyclability. We point out that performance might be further optimized by applying chemical and engineering strategies demonstrated for other MX_2 materials[11]. Our work opens the door to the use of this type of catalyst, and lays out a compelling scheme for assessing activity in similar classes of materials.

Methods

Computational details. Spin-polarized density functional theory calculations were performed using projector augmented wave (PAW) pseudopotentials[39,40] and the Perdew–Burke–Ernzerhof (PBE) exchange–correlation functional[41], as implemented in VASP[42,43]. All structures were based on MX_2 monolayers, and were relaxed until the force on each atom is less than 0.01 eV $Å^{-1}$. Vacuum space

in the direction perpendicular to the basal plane was kept to >15 Å. The adsorption energy E_a is defined as

$$E_a = E(\mathrm{H} + \mathrm{MX_2}) - E(\mathrm{MX_2}) - E(\mathrm{H_2})/2 \quad (1)$$

where $E(\mathrm{H} + \mathrm{MX_2})$, $E(\mathrm{MX_2})$ and $E(\mathrm{H_2})$ are the energies of H-adsorbed MX_2, pure MX_2 and an H_2 molecule, respectively. E_a was calculated using a 4 × 4 supercell. $\varepsilon_{\mathrm{LUS}}$ was calculated on the basis of the primitive cell. For the HER at pH = 0 and at zero potential relative to the standard hydrogen electrode, the free energy of $H^+ + e^-$ is by definition the same as that of 1/2 H_2 at standard conditions. Using this value as a zero reference, we estimate the free energy as

$$G_{\mathrm{tot}} = (E_a + E_{\mathrm{ZP}} - TS + E_{\mathrm{solv}})n_{\mathrm{H}} \quad (2)$$

where E_{ZP} is the zero-point energy, TS is the entropy contribution, and E_{solv} is the solvation energy. E_{solv} was evaluated using the VASPsol implementation of the implicit solvation model of ref. 44. Coverage-dependent values of G_{tot} for H-TaS_2, H-VS_2 and H-NbS_2 can be found in Supplementary Fig. 3. The differential free energy G_{diff} at the equilibrium H coverage represents the free energy cost to adsorb/desorb H on/from the catalyst, which in turn reflects the kinetics of catalysis near equilibrium[2,10,20,45]:

$$G_{\mathrm{diff}} = \partial G_{\mathrm{tot}}/\partial n_{\mathrm{H}} \quad (3)$$

Calculations of G_{diff} were performed at H/M = 1:16 for MX_2 surfaces, H/M = 1:2 for MoS_2 edges[10] and H/M = 1:1 for M = Pt, Ni (the last case was based on calculations of G_{tot} for Pt and Ni that showed equilibrium monolayer surface coverages). Corresponding plots can be found in Supplementary Fig. 3. We have also assessed the possible effect of interface polarization due to an applied potential by including a large electric field (~0.7 V nm^{-1}) pointing towards the substrate. Even with such a high field strength, the effect on G_{diff} is negligible, and our conclusion of high surface activity for group-5 MX_2 remains robust.

Synthesis. H-TaS_2 and H-NbS_2 crystal platelets were grown by chemical vapour deposition on SiO_2/Si substrates in a three-stage furnace. H-TaS_2 was derived from sulfur and tantalum chloride powders precursors under gaseous hydrogen purging via the following reactions:

$$\mathrm{H_2} + 1/8\mathrm{S_8} \rightarrow \mathrm{H_2S}$$

$$\mathrm{TaCl_5} + 2\mathrm{H_2S} + 1/2\mathrm{H_2} \rightarrow \mathrm{TaS_2} + 5\mathrm{HCl}$$

The sulfur, tantalum chloride and growth substrate regions were held respectively at ~250 °C, ~300 °C and ~750 °C for a 10 min growth period with a 20 sccm flow of Ar/H_2 (85:15 by volume). H-TaS_2 platelets were converted to the T phase by heating in a S/Ar atmosphere at 900 °C for 1 h and then rapidly quenching. H-NbS_2 crystal platelets were grown in the same way as H-TaS_2 except that $NbCl_5$ was used as the Nb element precursor and the substrate was held at 550 °C. Specifically, the $NbCl_5$ powder and S powder were placed in two different zones with temperatures of 250 °C and 300 °C, respectively, while the SiO_2/Si substrate was located in a third zone downstream with the temperature held at 550 °C. The carrier gas (Ar/H_2 85:15 by volume) and flow rate (20 sccm) were the same as those for H-TaS_2 growth. Multiple sample batches were prepared and tested.

T-MoS_2 nanosheets were prepared from commercial H-MoS_2 plates (Sigma-Aldrich)[30,46] by n-butyl lithium insertion and reaction with water.

Material characterization. SEM images and EDS were recorded on an FEI Quanta 400 microscope. XPS spectra were collected using a PHI Quantera X-ray photoelectron spectrometer. AFM measurements were taken using an Agilent Picoscan 5500 AFM equipped with a silicon tapping mode tip (AppNano). To compare the morphology before and after potential cycling, SEM and AFM images were taken on samples loaded onto glassy carbon plates. TEM images were collected on a JEOL 2100F TEM. Samples were prepared by drop-drying a diluted suspension in isopropanol onto copper grids covered with lacy carbon films. X-ray diffraction (XRD) was carried out on a Rigaku D/Max Ultima II Powder XRD. Our CVD-synthesized NbS_2 is not dense enough for powder XRD measurements, leading to an unreliably low signal-to-noise ratio. Raman spectra were taken at an excitation wavelength of 514 nm. The Raman spectra show that both TaS_2 and NbS_2 are 2H phase[47] (here 2 means the unit cell of bulk material has two layers, and H indicates a hexagonal atomic patterning in each layer). For comparison, the 1T phase reports peaks at ~285, ~417 and ~607 nm (ref. 48); and the 3R phase reports peaks at 290 ± 5, 330 ± 3, 386 ± 2 and 458 ± 3 nm (ref. 47), neither of which is consistent with our data.

Electrode preparation. The materials were transferred from the SiO_2/Si wafers by a PMMA transfer method. First, PMMA was spin-coated onto the wafers. The PMMA-covered wafer was etched in KOH solution, which removed the SiO_2 layer. Next, the PMMA was dissolved in acetone. Finally, the catalyst materials were isolated by centrifuging at 10,000 r.p.m. (relative centrifugal force 10,612g) for 5 min followed by drying in a N_2 atmosphere. A catalyst ink was made by mixing the obtained TaS_2/NbS_2, isopropanol, deionized water and Nafion (0.5 wt%) and sonicating for 30 min. The catalyst ink was then dropped onto a glassy carbon electrode, which served as the working electrode. The resulting catalyst loadings for H-TaS_2 and H-NbS_2 electrodes were ~55 and ~10 μg cm^{-2}, respectively. The catalyst loadings for all electrodes are listed in Supplementary Table 1.

Electrochemical performance. Electrochemical measurements were performed in a three-electrode electrochemical cell using an Autolab PGSTAT302N potentiostat. All measurements were performed in 50 ml of 0.5 M H_2SO_4 (aq.) electrolyte (pH = 0.16) prepared using 18 MΩ deionized water purged with Ar gas (99.999%). The glassy carbon electrode (CH Instruments, Dia. 3 mm) cast by the samples was employed as the working electrode and a saturated calomel electrode (SCE) (CH Instruments) was used as a reference electrode. A graphite rod (Alfa Aesar) was used as the counter electrode. A glassy carbon plate loaded with H-TaS_2 or H-NbS_2 samples was also employed as a working electrode to monitor the morphology change during potential cycling. As a comparison, carbon-supported Pt (Pt/C, 20%, Alfa Aesar) was also tested under identical conditions with a Pt loading of 25 μg cm^{-2}. The electrolyte was stirred through use of a magnetic stir bar during the electrochemical test to improve the mass transport. The SCE was calibrated in the high-purity H_2-saturated electrolyte using platinum as both working and counter electrode. Cyclic voltammetry was run at a scan rate of 1 mV s^{-1}, and the average of the two potentials at which the current crossed zero was taken to be the thermodynamic potential for the HER. All reported potentials are referenced to RHE. In 0.5 M H_2SO_4, E(RHE) = E(SCE) + 0.254 V. HER activity was measured using linear sweep voltammetry between +0.10 and −0.50 V versus RHE with a scan rate of 5 mV s^{-1}. The stability was evaluated by the potential cycling performed using cyclic voltammetry initiating at +0.2 V and ending at −0.6 V versus RHE at either 100 mV s^{-1} or 5 mV s^{-1}. All data were corrected for a small ohmic drop measured by EIS.

Additional characterization. EIS was performed at a bias potential of −0.1 V versus RHE while sweeping the frequency from 1 MHz to 10 mHz with a 5 mV a.c. amplitude. The EIS data were fitted to a Randles equivalent circuit consisting of an ohmic resistance R_{ohm} in series with a charge-transfer resistance (R_{ct})/constant-phase element (CPE) parallel combination. R_{ct} was also confirmed to scale with the exponential of the overpotential, further verifying its assignment as charge-transfer resistance. The power n of the CPE was found to fall within the range 0.68–0.78, indicating that frequency dispersion probably connected to porosity, surface roughness and/or diffusion factors. The effective double-layer capacitance C_{eff} was computed as $C_{\mathrm{eff}} = 1/R_{\mathrm{ct}} \times (QR_{\mathrm{ct}})^{1/n}$, where Q is the CPE coefficient. This formula is intended to partially account for the CPE frequency dispersion. Although the low values of n make precise determination of the electrolyte-accessible catalyst surface area difficult, the qualitative scaling behaviour with cycling can be safely assessed given the magnitude of the associated increases. For example, after 5,000 cycles, $(1/R_{\mathrm{ct}} \times R_{\mathrm{ct}}^{1/n})$ for H-TaS_2 changes by a factor of 3.6, compared with ~1,800 for Q, confirming that the scaling of the capacitance is not a by-product of decreased R_{ct} but rather is chiefly associated with increased surface area. Scaling plots of current versus C_{eff} (normalized by the initial values) for H-TaS_2 can be found in Supplementary Fig. 5.

The in-plane and out-of-plane resistivity of H-TaS_2 and H-MoS_2 were measured by I–V curves and the devices were fabricated through assistance of electron-beam lithography. The anisotropy of the electrical resistance was confirmed by direct resistivity measurements on pre-cycled samples of H-TaS_2 (see Supplementary Fig. 4), which yielded 8 Ω cm for out-of-plane resistivity compared with 3 × 10^{-5} Ω cm for in-plane resistivity (for comparison, H-MoS_2 demonstrated much larger in-plane resistivity of 1.7 Ω cm).

To measure the Faradaic efficiency and confirm H_2 as the reaction product, a gas-tight electrochemical set-up with two burettes filled with electrolyte solution (one for H_2 collection and one for O_2 collection) was applied to collect and periodically measure the increased gas volume due to H_2 generation in the HER compartment by H-TaS_2. The collected gas was further confirmed by gas chromatography (Shimadzu GC-2010 Plus) with a Carboxen 1010 PLOT column and a thermal conductivity detector by direct injection. As shown in Supplementary Fig. 9, the periodical measurement of H_2 production rate matches well with the theoretical value calculated from the charges passed under −0.4 V versus RHE (not iR-corrected). H_2 production for the first 5 h during the activation process continuously increased up to ~6.9 ml (0.31 mmol, compared with a theoretical yield of 7.7 ml or 0.34 mmol), which accounts for ~90% of Faradaic efficiency (FE). A FE of ~94% was calculated on the basis of the

collection of gas (38 ml, theoretical yield should be 40.4 ml or 1.8 mmol) in the subsequent 19 h electrolysis.

Tests for Pt contamination. Inductively coupled plasma mass spectrometry was conducted on a Thermo Scientific ICAP Q instrument with a CETAC ASX-520 auto sampler. A platinum standard was prepared from Inorganic Ventures MS Pt-10 ppm. A glassy carbon electrode with the *H*-TaS_2 catalyst after 5,000 cycles was digested in aqua regia solution (EMD OmniTrace hydrochloric acid and nitric acid = 3:1 by volume) overnight. The resulting solution was diluted into 3.75% HCl, 1.25% HNO_3 for analysis, and the experiments were repeated three times. Comparable trace amounts of Pt were detected in the diluted TaS_2 sample as in the aqua regia solvent solution (0.004–0.005 ppb, compared with the detection limit of 0.003 ppb), indicating that the *H*-TaS_2 electrode is free of Pt contamination. Because CO easily and strongly adsorbs on the surface of Pt, CO stripping voltammetry was also used as a secondary quantitative measurement of any trace amount of Pt on the electrode. After 5,000 cycles, the CO stripping voltammogram for *H*-TaS_2 had exactly the same shape as the background and no CO oxidation peak was observed, indicating no contamination of the long-term cycled *H*-TaS_2 electrode.

Data availability. The data that support the plots within this paper and other findings of this study are available from the corresponding author upon reasonable request.

Received 17 October 2016; accepted 22 June 2017; published 31 July 2017

References

1. Turner, J. A. Sustainable hydrogen production. *Science* **305,** 972–974 (2004).
2. Greeley, J., Jaramillo, T. F., Bonde, J., Chorkendorff, I. & Norskov, J. K. Computational high-throughput screening of electrocatalytic materials for hydrogen evolution. *Nat. Mater.* **5,** 909–913 (2006).
3. Faber, M. S. & Jin, S. Earth-abundant inorganic electrocatalysts and their nanostructures for energy conversion applications. *Energy Environ. Sci.* **7,** 3519–3542 (2014).
4. McCrory, C. C. L. *et al.* Benchmarking hydrogen evolving reaction and oxygen evolving reaction electrocatalysts for solar water splitting devices. *J. Am. Chem. Soc.* **137,** 4347–4357 (2015).
5. Tavakkoli, M. *et al.* Single-shell carbon-encapsulated iron nanoparticles: synthesis and high electrocatalytic activity for hydrogen evolution reaction. *Angew. Chem. Int. Edn* **54,** 4535–4538 (2015).
6. Chhowalla, M. *et al.* The chemistry of two-dimensional layered transition metal dichalcogenide nanosheets. *Nat. Chem.* **5,** 263–275 (2013).
7. Karunadasa, H. I. *et al.* A molecular MoS_2 edge site mimic for catalytic hydrogen generation. *Science* **335,** 698–702 (2012).
8. Jaramillo, T. F. *et al.* Identification of active edge sites for electrochemical H_2 evolution from MoS_2 nanocatalysts. *Science* **317,** 100–102 (2007).
9. Kibsgaard, J., Chen, Z., Reinecke, B. N. & Jaramillo, T. F. Engineering the surface structure of MoS_2 to preferentially expose active edge sites for electrocatalysis. *Nat. Mater.* **11,** 963–969 (2012).
10. Hinnemann, B. *et al.* Biomimetic hydrogen evolution: MoS_2 nanoparticles as catalyst for hydrogen evolution. *J. Am. Chem. Soc.* **127,** 5308–5309 (2005).
11. Benck, J. D., Hellstern, T. R., Kibsgaard, J., Chakthranont, P. & Jaramillo, T. F. Catalyzing the hydrogen evolution reaction (HER) with molybdenum sulfide nanomaterials. *ACS Catal.* **4,** 3957–3971 (2014).
12. Lu, Q., Yu, Y., Ma, Q., Chen, B. & Zhang, H. 2D transition-metal-dichalcogenide-nanosheet-based composites for photocatalytic and electrocatalytic hydrogen evolution reactions. *Adv. Mater.* **28,** 1917–1933 (2016).
13. Zhang, X., Lai, Z., Tan, C. & Zhang, H. Solution-processed two-dimensional MoS_2 nanosheets: preparation, hybridization, and applications. *Angew. Chem. Int. Edn* **55,** 8816–8838 (2016).
14. Chen, J. *et al.* One-pot synthesis of CdS nanocrystals hybridized with single-layer transition-metal dichalcogenide nanosheets for efficient photocatalytic hydrogen evolution. *Angew. Chem. Int. Edn* **54,** 1210–1214 (2015).
15. Miao, J. *et al.* Hierarchical Ni–Mo–S nanosheets on carbon fiber cloth: a flexible electrode for efficient hydrogen generation in neutral electrolyte. *Sci. Adv.* **1,** e1500259 (2015).
16. Schmickler, W. & Santos, E. *Interfacial Electrochemistry* 2nd edn (Springer, 2010).
17. Santos, E., Quaino, P. & Schmickler, W. Theory of electrocatalysis: hydrogen evolution and more. *Phys. Chem. Chem. Phys.* **14,** 11224–11233 (2012).
18. Trasatti, S. Work function, electronegativity, and electrochemical behaviour of metals: III. Electrolytic hydrogen evolution in acid solutions. *J. Electroanal. Chem. Interfacial Electrochem.* **39,** 163–184 (1972).
19. Calle-Vallejo, F., Koper, M. T. M. & Bandarenka, A. S. Tailoring the catalytic activity of electrodes with monolayer amounts of foreign metals. *Chem. Soc. Rev.* **42,** 5210–5230 (2013).
20. Nørskov, J. K. *et al.* Trends in the exchange current for hydrogen evolution. *J. Electrochem. Soc.* **152,** J23–J26 (2005).
21. Liu, Y., Wang, Y. M., Yakobson, B. I. & Wood, B. C. Assessing carbon-based anodes for lithium-ion batteries: a universal description of charge-transfer binding. *Phys. Rev. Lett.* **113,** 028304 (2014).
22. Arikado, T., Iwakura, C. & Tamura, H. Some oxide catalysts for the anodic evolution of chlorine: reaction mechanism and catalytic activity. *Electrochim. Acta* **23,** 9–15 (1978).
23. Arikado, T., Iwakura, C. & Tamura, H. A consideration of the electrochemical mechanism in the chlorine evolution reaction. *Electrochim. Acta* **23,** 799–801 (1978).
24. Suntivich, J. *et al.* Design principles for oxygen-reduction activity on perovskite oxide catalysts for fuel cells and metal–air batteries. *Nat. Chem.* **3,** 546–550 (2011).
25. Pan, H. Metal dichalcogenides monolayers: novel catalysts for electrochemical hydrogen production. *Sci. Rep.* **4,** 5348 (2014).
26. Tsai, C., Chan, K., Nørskov, J. K. & Abild-Pedersen, F. Theoretical insights into the hydrogen evolution activity of layered transition metal dichalcogenides. *Surf. Sci.* **640,** 133–140 (2015).
27. Yuan, J. *et al.* Facile synthesis of single crystal vanadium disulfide nanosheets by chemical vapor deposition for efficient hydrogen evolution reaction. *Adv. Mater.* **27,** 5605–5609 (2015).
28. Voiry, D. *et al.* Enhanced catalytic activity in strained chemically exfoliated WS_2 nanosheets for hydrogen evolution. *Nat. Mater.* **12,** 850–855 (2013).
29. Lukowski, M. A. *et al.* Enhanced hydrogen evolution catalysis from chemically exfoliated metallic MoS_2 nanosheets. *J. Am. Chem. Soc.* **135,** 10274–10277 (2013).
30. Voiry, D. *et al.* Conducting MoS_2 nanosheets as catalysts for hydrogen evolution reaction. *Nano Lett.* **13,** 6222–6227 (2013).
31. Zeng, Z., Tan, C., Huang, X., Bao, S. & Zhang, H. Growth of noble metal nanoparticles on single-layer TiS_2 and TaS_2 nanosheets for hydrogen evolution reaction. *Energy Environ. Sci.* **7,** 797–803 (2014).
32. Gupta, U., Rao, B. G., Maitra, U., Prasad, B. E. & Rao, C. N. R. Visible-light-induced generation of H_2 by nanocomposites of few-layer TiS_2 and TaS_2 with CdS nanoparticles. *Chem. Asian J.* **9,** 1311–1315 (2014).
33. Fletcher, S. Tafel slopes from first principles. *J. Solid State Electrochem.* **13,** 537–549 (2009).
34. Zeradjanin, A. R., Ventosa, E., Bondarenko, A. S. & Schuhmann, W. Evaluation of the catalytic performance of gas-evolving electrodes using local electrochemical noise measurements. *ChemSusChem* **5,** 1905–1911 (2012).
35. Gao, L. *et al.* Repeated growth and bubbling transfer of graphene with millimetre-size single-crystal grains using platinum. *Nat. Commun.* **3,** 699 (2012).
36. Wang, Y. *et al.* Electrochemical delamination of CVD-grown graphene film: toward the recyclable use of copper catalyst. *ACS Nano* **5,** 9927–9933 (2011).
37. Murphy, D. W. *et al.* Properties of H_xTaS_2: correlation between the superconducting T_c and an electronic instability in layer compounds. *J. Chem. Phys.* **62,** 967–972 (1975).
38. Murphy, D. W. & Hull, G. W. Monodispersed tantalum disulfide and adsorption complexes with cations. *J. Chem. Phys.* **62,** 973–978 (1975).
39. Blöchl, P. E. Projector augmented-wave method. *Phys. Rev. B* **50,** 17953–17979 (1994).
40. Kresse, G. & Joubert, D. From ultrasoft pseudopotentials to the projector augmented-wave method. *Phys. Rev. B* **59,** 1758–1775 (1999).
41. Perdew, J. P., Burke, K. & Ernzerhof, M. Generalized gradient approximation made simple. *Phys. Rev. Lett.* **77,** 3865–3868 (1996).
42. Kresse, G. & Furthmüller, J. Efficient iterative schemes for *ab initio* total-energy calculations using a plane-wave basis set. *Phys. Rev. B* **54,** 11169–11186 (1996).
43. Kresse, G. & Hafner, J. *Ab initio* molecular dynamics for liquid metals. *Phys. Rev. B* **47,** 558–561 (1993).
44. Mathew, K., Sundararaman, R., Letchworth-Weaver, K., Arias, T. A. & Hennig, R. G. Implicit solvation model for density-functional study of nanocrystal surfaces and reaction pathways. *J. Chem. Phys.* **140,** 084106 (2014).
45. Tsai, C., Abild-Pedersen, F. & Nørskov, J. K. Tuning the MoS_2 edge-site activity for hydrogen evolution via support interactions. *Nano Lett.* **14,** 1381–1387 (2014).
46. Kappera, R. *et al.* Phase-engineered low-resistance contacts for ultrathin MoS_2 transistors. *Nat. Mater.* **13,** 1128–1134 (2014).

47. McMullan, W. G. & Irwin, J. C. Raman scattering from 2H and 3R–NbS_2. *Solid State Commun.* **45,** 557–560 (1983).
48. Carmalt, C. J., Manning, T. D., Parkin, I. P., Peters, E. S. & Hector, A. L. Formation of a new (1T) trigonal NbS_2 polytype via atmospheric pressure chemical vapour deposition. *J. Mater. Chem.* **14,** 290–291 (2004).

Acknowledgements

We thank W. Zhou (ORNL), W. I. Choi (LLNL), A. Mohite and G. Gupta (LANL) for valuable discussions. B.C.W. and Y.L. acknowledge funding from LLNL LDRD Grant 12-ERD-053, with computing support from the LLNL Institutional Computing Grand Challenge Program. T.O. and B.C.W. acknowledge additional support from the US Department of Energy (DOE) Fuel Cell Technologies Office. Y.M.W. acknowledges the UCOP funding support on mesoscopic 2D materials. A portion of this work was performed under the auspices of the US DOE by LLNL under Contract DE-AC52-07NA27344. K.P.H. acknowledges funding from PIRE-2 Grant OISE-0968405. J.W. and K.K. acknowledge funding from MURI 2D Grant W911NF-11-1-0362. Y.Y., J.Z. and J.L. acknowledge support from the Welch Foundation grant C-1716. Y.L. and B.I.Y. acknowledge support from the Office of Naval Research Grant N00014-15-1-2372 and the Army Research Office Grant W911NF-16-1-0255. This work used computing resources sponsored by the DOE Office of EERE at NREL, and the NSF XSEDE Grant ACI-1053575.

Author contributions

Y.L. conceived the idea and performed the theory calculations with guidance from T.O., B.C.W. and B.I.Y. K.P.H. synthesized the samples. J.W. performed the electrochemical testing. J.W. and K.P.H. performed a majority of the materials characterization, under the guidance of R.V., J.L. and P.M.A. Other authors provided additional sample characterization.

Additional information

Supplementary information is available for this paper.

Reprints and permissions information is available at www.nature.com/reprints.

Correspondence and requests for materials should be addressed to B.C.W. or B.I.Y.

How to cite this article: Liu, Y. *et al.* Self-optimizing, highly surface-active layered metal dichalcogenide catalysts for hydrogen evolution. *Nat. Energy* **2**, 17127 (2017).

Competing interests

The authors declare no competing financial interests.